

Muon counting with the Underground Muon Detector of The Pierre Auger Observatory

Marina Scornavacche^{1,2,*} for the Pierre Auger Collaboration^{3,**}

¹Instituto de Tecnologías en Detección y Astropartículas, Av. Gral Paz 1499, 1650 Buenos Aires, Argentina

²Institut für Astroteilchenphysik, Hermann-von-Helmholtz-Platz 1, 76131 Karlsruhe, Germany

³Observatorio Pierre Auger, Av. San Martín Norte 304, 5613 Malargüe, Argentina

Abstract. The Underground Muon Detector (UMD) aims to extend the detection range of the Pierre Auger Observatory to observe cosmic rays of energies greater than $10^{16.6}$ eV and performs a direct measurement of the muon component (sensitive observable to the mass composition) of the air showers. In this work, we will present an overview of the final design of the UMD and its reconstruction techniques alongside the observations obtained during the engineering array phase. First results suggest that the current hadronic interaction models have a muon deficit at energies between 2×10^{17} eV and 2×10^{18} eV.

1 Introduction

The Pierre Auger Observatory was designed to answer the key questions about the origin and composition of ultra-high energy cosmic rays. The Observatory is currently undergoing an upgrade dubbed *AugerPrime* [1]. The purpose of *AugerPrime* is to improve the sensitivity to mass composition observables, such as the muon content of the air showers. In order to probe the characteristics of cosmic rays above 10^{17} eV, *AugerPrime* will provide a cleaner separation between the electromagnetic and muonic components of the showers. The Underground Muon Detector (UMD) plays a key role in *AugerPrime* since it is designed to perform a direct measurement of the muon component of the air showers.

In the framework of the Heitler-Matthews model of a cascade [2], the number of muons N_μ is a composition sensitive observable since it scales with energy E and mass number A as $N_\mu \propto \frac{AE^\beta}{(A\xi_c)^\beta}$, where ξ_c is the critical energy at which charged pions are likely to decay into muons ($\xi_c \sim 20 - 30$ GeV, $\beta \sim 0.9$). Assuming the validity of the superposition model, the number of muons can be written as $N_\mu^A = A^{1-\beta} N_\mu^p$ indicating that more muons are produced in an iron shower than in a proton shower at the same total primary energy.

2 The underground muon detector: Final design and current production status

The Pierre Auger Observatory consists of a surface detector of about 1660 water-Cherenkov stations distributed in a triangular grid with 1500 m spacing (SD-1500) covering

a total area of 3000 km². To extend the energy threshold of the SD to lower energies, two denser arrays with spacings of 750 m (SD-750) and 433 m (SD-433) were deployed (over areas of 23.5 km² and 1.9 km², respectively). The two arrays SD-750 and SD-433 will be equipped with UMDs. Currently, 26 positions (37% of the full UMD array) are in acquisition (see Figure 1). The full UMD array is expected to be completed by end-2023.

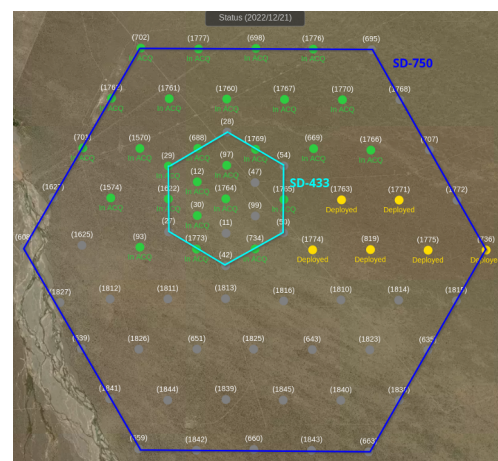


Figure 1. Schematics of the water-Cherenkov surface detectors (circles) where UMD positions were deployed (yellow) and are in acquisition (green) in the SD-750 (blue grid) and SD-433 (light blue grid).

In the final design, three modules of 10 m² are buried at 2.3 m next to a water-Cherenkov detector of the SD-750 and the SD-433 (see Figure 2). The soil shielding ensures the exclusive detection of the muon content of the air showers. Each module consists of 64 plastic scintillator strips containing wavelength shifting optical fiber con-

*e-mail: marina.scornavacche@iteda.cnea.gov.ar

**e-mail: spokespersons@auger.org, full author list available at https://www.auger.org/archive/authors_2022_10.html

nected to an array of 64 silicon photomultipliers (SiPMs). When a muon impinges the scintillator, the photons produced are collected and propagated along the fibers to the photodetector. In Figure 3, an image of a complete deployed station is shown, along with a module under construction.

For the full UMD array, the SiPM option was chosen because of their better photodetection efficiency, reduced power consumption and lower cost [3]. Each SiPM is an array of 1584 avalanche photo-diodes (also referred to as cells) operated in Geiger mode, where the number of triggered cells is referred to as photon equivalents (PE). For a detailed review of the design, characterization and implementation of the SiPMs for the data acquisition see references [4][5].

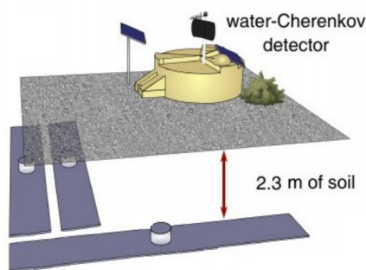


Figure 2. Schematics of the final UMD design with three modules of 10 m².

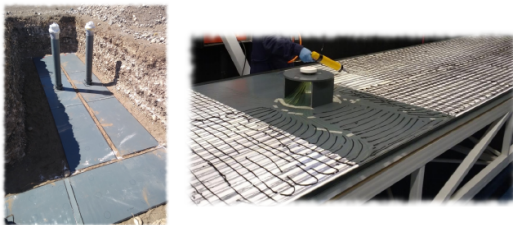


Figure 3. (Left) Three modules of 10 m² deployed in the field. (Right) Scintillator module constructed in the assembly building.

In the final design, the number of muons can be estimated in two complementary ways: *counting* and *integrated signal*. The first relies on the amplitude of the signals, the latter on its charge. The two modes work in a complementary way to extend the dynamic range of the detector: *counting* for low particle densities (far from the shower core) and *integrated signal* for high particle densities (close to the shower core).

In the *counting* mode the 64 SiPMs signals are handled independently through a pre-amplifier, fast-shaper, and a discriminator. A “1-bit” is produced if the signal goes above the discriminator threshold and “0-bit” otherwise. An example of a simulated single-muon signal [6] is shown in Figure 4 (top). This discriminator threshold is set at 2.5 photon equivalents (PE) to filter most of the SiPM dark current (due to the crosstalk between the SiPM cells). The calibration procedure [7] ensures an equalized response in the whole SiPM array.

The single-muon signal in the *counting* mode was characterized employing laboratory measurements. Muons deposit wider signals than the background in the binary trace, so muons can be identified as sequences of ‘1111x’. Muons are then identified by applying a time window starting from the first identified match, during which the muon search is inhibited. The *counting* strategy was proposed as a compromise between the under-counting due to the strip efficiency and over-counting due to both the detector noise and wide muon signals. An optimal inhibition window of 12 samples from the first match was selected, since it can completely contain approximately 99% of the muon signals.

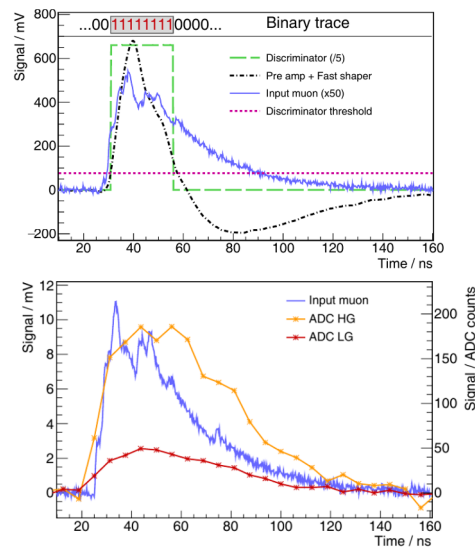


Figure 4. Two simulated single-muon signal at 2 m for the *Counting* mode (top) and for the *Integrated signal* mode (bottom). In the first case, the signal from the SiPM and the discriminator pulse are re-scaled for illustration.

In the *integrated signal* mode, the 64 SiPMs signals are summed [4], and the output is the total signal charge. The number of muons can be obtained by dividing the signal charge by the mean charge deposit of a single muon. Two independent channels are employed: a high gain (HG) and a low gain (LG) (see Figure 4 (bottom)). An algorithm is implemented in the electronics to extract the calibration histograms [8]. The calibration histograms are built for each channel selecting individual muons with the counting mode. An example is shown in Figure 5. The performance and calibration of the detectors are constantly being monitored to ensure high quality data.

The results obtained with the *counting* mode strategy from the UMD engineering array [9] will be shown in section 3. Currently, improvements have been made in the low level reconstruction of the *integrated signal* mode. Regarding the *counting* mode, a new *counting* strategy has been developed [10] that generates a smaller standard deviation of the estimated number of muons at high input number of muons and that reconstructs the time structure of the muon signal to a single time-bin resolution, opening the door to new studies of the temporal structure. UMDs

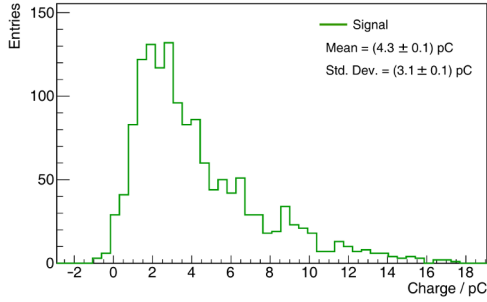


Figure 5. Example of a single muon charge histogram used to calibrate the *integrated signal mode*.

will significantly increase the amount of high quality data. These improvements will ensure high-level physics analyses with the data.

3 Results from engineering array

A data set of 1742 events measured by the UMD engineering array [9] was selected, with energies of $[2 \times 10^{17}, 2 \times 10^{18}]$ eV and $\theta \leq 45^\circ$. These cuts allow us to minimize uncertainties and to work in a regime of full efficiency. The data used correspond to a 1-year period.

The deposited muon density $\rho(r)$ is modeled with a muon lateral distribution function (MLDF) at a perpendicular distance r to the shower axis. The optimal distance to minimize the uncertainties of the signal is 450 m. An average MLDF is determined from Monte-Carlo simulations of extensive air showers and the signal deposited by an event is adjusted to this average by scaling its normalization in a fitting procedure. On an event-by-event basis, the value of $\rho(450)$ is estimated with a maximum likelihood. For a detailed description of the likelihood method, see reference [9]. An example of the MLDF for an event is shown in Figure 6.

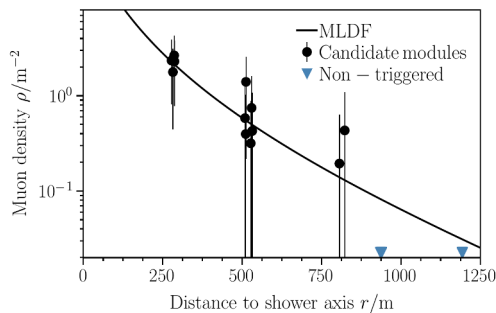


Figure 6. Example of a MLDF fit to a real event.

The muon density estimator is corrected for attenuation $\rho_{35} = \rho(450)/f_{att}(\theta)$ (for the soil and the longer path in the atmosphere) based on the constant intensity cut method [11]. The reconstructed attenuation-free muon density ρ_{35} is shown in Figure 7 as a function of the energy estimated by the SD. In this energy range, a single power-law dependence of ρ_{35} with energy is expected from Monte-Carlo

simulations. Hence, a fit of such a kind was performed and is also shown in Figure 7.

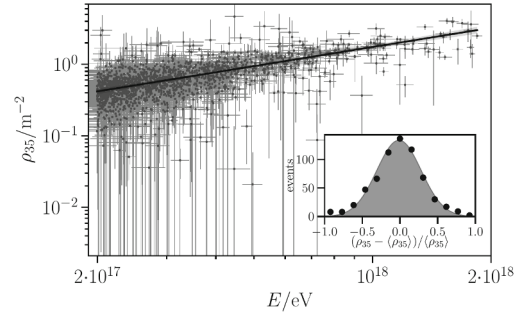


Figure 7. Experimental muon density estimator ρ_{35} (dots) as a function of the reconstructed energy, and a single power-law fit (line). (Inset) The distribution of the normalized residuals.

The evolution of the muon content in data is compared to simulations of proton (red) and iron (blue) primaries in Figure 8. The muon densities are normalized by the energy. The number of events in each energy bin is stated at the top of the figure. The obtained fit curve is shown as the black solid line with a shaded band corresponding to the statistical uncertainties. The systematic uncertainties are indicated by square brackets, corresponding 14% to the SD energy estimate. The muon densities are larger in data than in the models. However, a shift of the data points within the systematic uncertainties (mainly inherited from the energy scale) is enough to bring them in the region of the iron primaries.

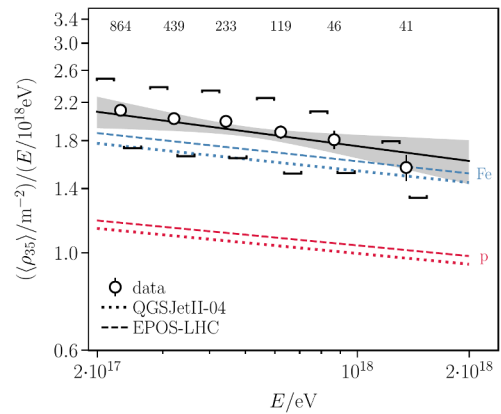


Figure 8. Energy-normalized muon densities compared to the expectations from simulations using QGSJetII-04 (dotted) and EPOS-LHC (dashed).

The depth of the shower maximum X_{max} can be directly observed with the fluorescence detectors (FD). In the generalised Heitler model, $\langle \ln \rho_{35} \rangle$ and $\langle X_{max} \rangle$ are linear with the mean logarithmic mass $\langle \ln A \rangle$. With the $\langle X_{max} \rangle$ data extracted from [12] we obtained Figure 9. For the EPOS-LHC model to explain the data, an increase of 38% in the muon density is required at $10^{17.5}$ eV and 10^{18} eV, while for QGSJetII-04, an increment of 50% and 53% is needed.

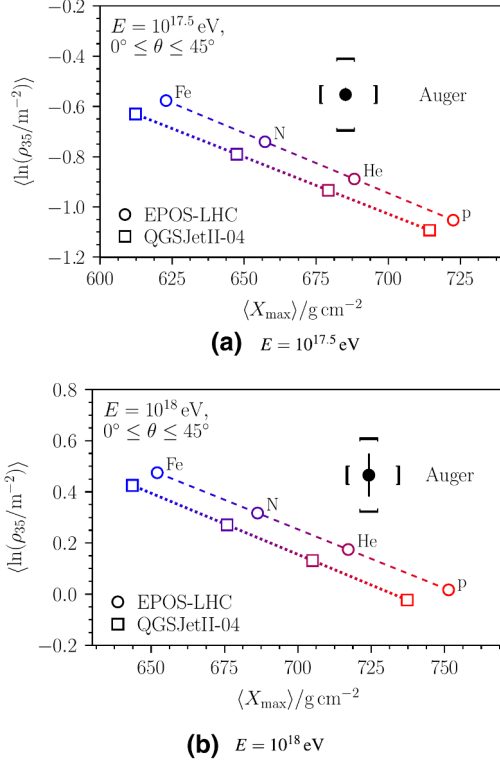


Figure 9. Mean logarithmic muon density $\langle \ln \rho_{35} \rangle$ as a function of the mean depth of the shower maximum $\langle X_{\max} \rangle$ for simulations with primary energies of $10^{17.5}$ eV (a) and 10^{18} eV (b) compared to Auger data.

The z -scale factor is defined by the following equation

$$z = \frac{\langle \ln x \rangle - \langle \ln x \rangle_{\text{p}}}{\langle \ln x \rangle_{\text{Fe}} - \langle \ln x \rangle_{\text{p}}}, \quad (1)$$

where x is the muon-density estimator and the symbols $\langle \cdot \rangle_{\text{p}}$ and $\langle \cdot \rangle_{\text{Fe}}$ represent the expected muon densities for proton and iron showers, simulated with a given model and accounting for detector effects.

We can extend previous results in inclined air showers at higher energies [13] with the z -scale factor, where x is the muon-density estimator ρ_{35} (in this work) and R_{μ} (in ref. [13]). The measurements of $\langle X_{\max} \rangle$ by the FD can be converted into the mean logarithmic mass $\langle \ln A \rangle$ assuming the validity of the superposition model and finally into the z -scale factor $z = \frac{\langle \ln A \rangle}{\ln 56}$.

The hadronic interaction models fail to reproduce the z -scale factor consistently, as shown in Figure 10. This tension is higher in the lower energies (this work) due to the smaller uncertainties. However, the results are sensitive to a change in energies. A positive shift of our energy scale within its systematic uncertainties would reduce the tensions on the muon numbers.

4 Conclusions

In this work, we present the first direct measurement by the Pierre Auger Collaboration of the muon content of air showers at energies between 2×10^{17} eV and 2×10^{18} eV.

We have shown that the hadronic interaction models indicate fewer muons are produced in simulated showers than those observed in extensive air showers. These results have extended previous results in inclined air showers at higher energies [13].

We have presented an overview of the final UMD design. Currently 37% of positions of the full UMD array have been installed and are in acquisition. The full UMD array will be completed by end-2023, increasing significantly the amount of UMD data available for performing high-level physics analyses.

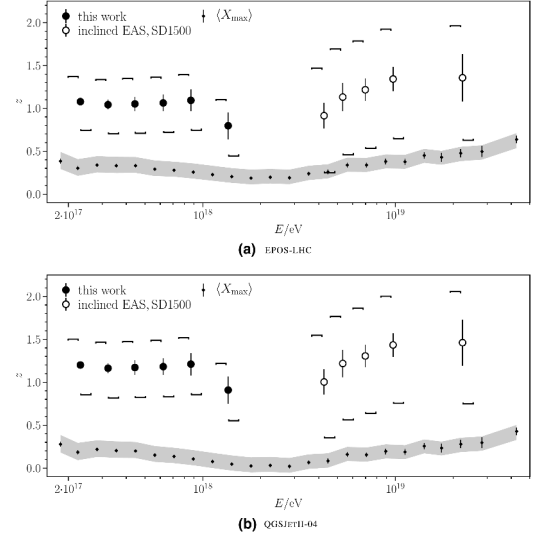


Figure 10. z -scale factor from this work (filled circles), from measurements of inclined air showers at higher energies (open circles) and from $\langle X_{\max} \rangle$ measurements with the FD.

References

- [1] A. Aab et al. [Pierre Auger Coll.], *Science Reviews* **1**, 8 (2020)
- [2] J. Matthews, *Astropart. Phys.* **22**, 387 (2005)
- [3] A. Aab et al. [Pierre Auger Coll.], *JINST* **12**, P03002 (2017)
- [4] A. Aab et al. [Pierre Auger Coll.], *JINST* **16**, P01026 (2021)
- [5] A. Aab et al. [Pierre Auger Coll.], *JINST* **16**, T07008 (2021)
- [6] A. Botti et al., *JINST* **16**, P07059 (2021)
- [7] A. Botti, *Proc. Int. Cosmic Ray Conf.* **37**, 233 (2021)
- [8] A. Aab et al. [Pierre Auger Coll.], *JINST* **16**, P04003 (2021)
- [9] A. Aab et al. [Pierre Auger Coll.], *Eur. Phys. J. C* **80**, 751 (2020)
- [10] F. Gesualdi, A. D. Supanitsky, *Eur. Phys. J. C* **82**, 925 (2022)
- [11] J. Hersil et al., *Phys. Rev. Lett.* **6**, 22 (1961)
- [12] J. Bellido, *Proc. Int. Cosmic Ray Conf.* **35**, 506 (2017)
- [13] A. Aab et al. [Pierre Auger Coll.], *Phys. Rev. D* **91**, 032003 (2015)